

Hui Zhang^a, Xiao-Fei Pan^a, Zhe-Feng Zhang^a, Jayanta Das^{b,c}, Ki Buem Kim^b, Clemens Müller^b, Falko Baier^b, Martin Kusy^c, Annett Gebert^c, Guo He^d, Jürgen Eckert^{b,c}

^aShenyang National Laboratory for Materials Science, Institute of Metal Research, Chinese Academy of Sciences, Shenyang, P. R. China

^bTechnische Universität Darmstadt, FB 11 Material- und Geowissenschaften, FG Physikalische Metallkunde, Darmstadt, Germany

^cIFW Dresden, Institut für Metallische Werkstoffe, Dresden, Germany

^dShanghai Jiaotong University, School of Materials Science and Engineering, Shanghai, P. R. China

Toughening mechanisms of a Ti-based nanostructured composite containing ductile dendrites

Dedicated to Professor Wolfgang Blum on the occasion of his 65th birthday

The compressive deformation behavior of a multi-component Ti–Cu–Ni–Sn–Nb composite containing ductile dendritic precipitates embedded in a nanostructured matrix was investigated. The Ti-based composite not only displays a high compressive plasticity of $\approx 21\%$, but also exhibits a high fracture strength of ≈ 1.8 GPa, which is comparable to that of monolithic bulk metallic glasses. Pronounced work hardening was observed after yielding. The surface deformation morphology reveals that the work-hardening behavior of the composite is related to the plastic deformation of the dendritic phase and the interaction of shear bands in the nanostructured matrix with the hardened dendrites. At the final stage of compression, most of the dendrites are work hardened, whereby the propagation of the shear bands in the matrix is retarded. The strong interaction between the dendrites and the matrix contributes to the high strength and plastic deformation capability of the composite. The fracture surface exhibits viscous flow traces, indicating that softening or melting of the composite occurs at the moment of fracture, due to the release of the high elastic energy stored in the specimen.

Keywords: Ti-based composite; Dendritic phase; Compressive plasticity; Shear bands; Work hardening

1. Introduction

Since Zr-based bulk metallic glasses (BMGs) with high glass-forming ability were successfully synthesized about ten years ago [1, 2], many interesting mechanical properties of bulk metallic glasses have been recognized [3, 4]. The major advantages that they offer are their high strength, low elastic modulus and good wear properties [3, 5]. Their fracture toughness is comparable to that of crystalline metals ($15\text{--}70$ MPa $m^{1/2}$) [6–8]. A unique relationship between the nominal applied stress intensity factor range ΔK

and the fatigue crack growth rate da/dN has been observed in some Zr-based BMGs [9–11]. However, the final fracture of these bulk metallic glasses happens catastrophically and involves very little overall plastic deformation under unconstrained loading conditions. The failure of these BMGs is concentrated in a highly localized shear band, reflecting a lack of work hardening of these materials. Different fracture mechanisms of metallic glasses under monotonic tension and compression have been explained by considering the combined effect of normal and shear stress [12, 13].

Until recent years, various attempts have been made to improve the ductility of the BMG materials while maintaining their high strength. For example, continuous tungsten fiber-reinforced Zr-based metallic glasses have been synthesized, which show improved plastic strain and fatigue life time [14, 15]. However, processing of the tungsten/metallic glass composite is difficult, and a homogeneous distribution of the tungsten fibers in the matrix is difficult to achieve.

In an in-situ formed Be-containing Zr-based metallic glass matrix/dendritic phase composite, a dramatic increase in plastic strain has been obtained under quasistatic tension and compression, providing an effective way to synthesize metallic glass composites with improved ductility [16, 17]. Moreover, substantially improved mechanical properties have also been obtained recently on an in-situ formed Ti-based nanostructure-dendrite composite with plastic strains larger than 15% and fracture stresses higher than 2 GPa [18]. The increased ductility of such composites is attributed to the dendrites dispersed in the matrix, acting as obstacles hindering the propagation of shear bands [19, 20]. The improved mechanical properties combined with the potential for engineering applications of these composites have prompted us to search for the mechanisms, which impart both improved strength and ductility. However, the deformation and fracture mechanisms of these composites have not been well understood, yet.

In this paper, we try to reveal the microscopic deformation behavior of a Ti-based nanostructured matrix/ductile

dendritic phase composite synthesized by simple arc-melting. The enhanced ductility of the Ti-based composite is discussed in terms of the deformation mechanisms of the ductile dendritic phase and its role in resisting the propagation of shear bands during compression.

2. Experimental

Master alloy ingots with nominal composition of $\text{Ti}_{62}\text{Cu}_{14}\text{Ni}_{12}\text{Sn}_4\text{Nb}_8$ (at.%) were prepared by arc-melting a mixture of Ti, Cu, Ni, Sn and Nb metals (purity 99.99 %) on a water-cooled copper hearth under an argon atmosphere. The samples were prepared by arc-melting the master alloy ingots several times until a homogeneous melt was formed and cooled at a slow rate.

The phases of the arc-melted samples were examined by X-ray diffraction (XRD) using a Rigaku diffractometer with $\text{Cu } K_\alpha$ radiation. The microstructure and the volume fraction of the dendritic phase were examined by a Cambridge S360 scanning electron microscope (SEM). Small parallelepiped compression specimens were cut by wire electrical discharge machining (WEDM) to 4 mm \times 4 mm cross-section and 8 mm height. The surfaces were carefully ground and polished allowing for the following observation of the surface deformation morphology. The specimens were monotonically compressed using a computer-controlled servohydraulic testing machine (MTS 810) at an initial strain rate of $1 \times 10^{-4} \text{ s}^{-1}$ (constant displacement rate) at room temperature in air ($\approx 295 \text{ K}$, 55 % relative humidity). The strain was determined after correcting for the stiffness of the testing machine. The compression tests were performed on at least two specimens with one specimen being compressed until fracture and the other one stopped and unloaded at different intervals during the test. After compression, the surface deformation morphology and the fractography of the specimens were examined using a S360 SEM.

3. Results and discussion

3.1. Phases and microstructure

Figure 1 shows X-ray diffraction patterns of the arc-melted $\text{Ti}_{62}\text{Cu}_{14}\text{Ni}_{12}\text{Sn}_4\text{Nb}_8$ sample. The two main phases are $\beta\text{-Ti(M)}$ ($\text{M} = \text{Nb}, \text{Sn}, \text{Cu}, \text{and Ni}$) and $\alpha\text{-Ti(M)}$ solid solu-

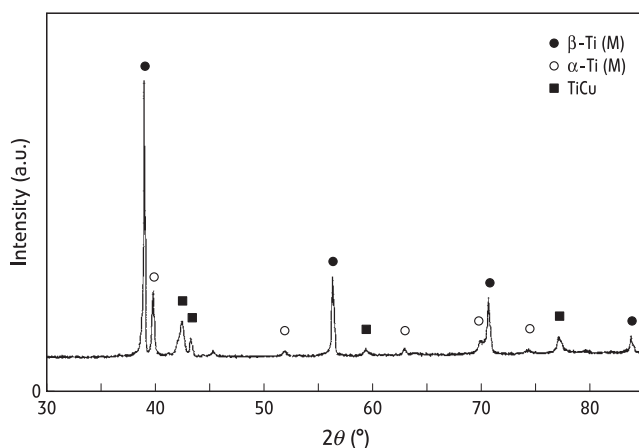


Fig. 1. X-ray diffraction pattern of the $\text{Ti}_{62}\text{Cu}_{14}\text{Ni}_{12}\text{Sn}_4\text{Nb}_8$ composite synthesized by arc-melting.

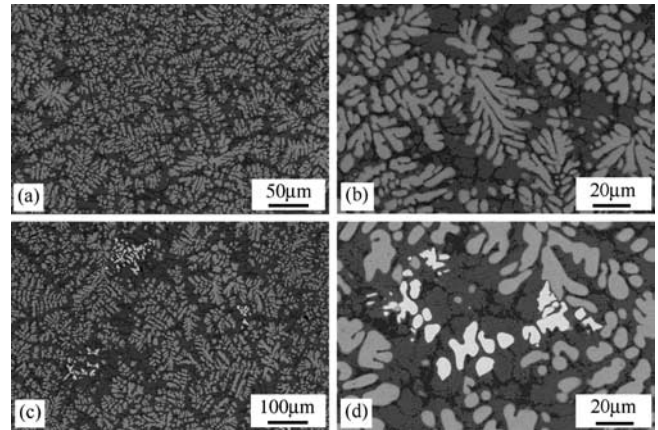


Fig. 2. Scanning electron micrographs (BSE contrast) of the $\text{Ti}_{62}\text{Cu}_{14}\text{Ni}_{12}\text{Sn}_4\text{Nb}_8$ composite showing: (a) and (b) morphology of the dendrites and the matrix; (c) and (d) white phase at local sites of the specimen surface.

tion, as marked by the filled and open circles, respectively. The other weaker diffraction peaks correspond to intermetallic TiCu . Figure 2a shows the microstructure of the arc-melted sample observed by SEM using the back-scattering technique (BSE contrast). Bright dendritic precipitates are homogeneously dispersed in a dark matrix. The matrix consists of gray and net-shaped black phases. The volume fraction of the gray phase is higher than that of the black phase, as clearly seen from Fig. 2b. Based on the microstructure observations and the XRD results, the dendritic phase can be identified as a body-centered cubic (bcc) $\beta\text{-Ti}$ solid solution. The dark matrix consists mainly of $\alpha\text{-Ti}$ solid solution and a limited amount of intermetallic TiCu as identified from the XRD pattern. From the SEM images, the volume fraction of the dendritic phase is determined to be around 30 %. A transmission electron microscopy (TEM) study of a similar Ti-based alloy has revealed that the gray matrix consists mainly of nanometer-sized grains with eutectic structure [21]. Accordingly, the alloy studied here is a nanostructured composite reinforced by the dendritic phase.

The different phase contrast observed in the dendrite and matrix phases corresponds to different compositions, which were analysed by energy-dispersive X-ray (EDX) analysis and are listed in Table 1. The matrix phases are enriched in Ni and Cu, but depleted in Sn and Nb, whereas the dendrites are Sn- and Nb-rich phase, but depleted in Ni and Cu. Compared to the gray dendritic phase, there is only a small amount of white dendritic phase (Fig. 2c) in the Ti-based alloys. The white dendritic phase has the same morphology but different contrast than the gray dendritic phase, as shown by an enlarged view in Fig. 2d. EDX analysis re-

Table 1. Results of the EDX analysis of the $\text{Ti}_{62}\text{Cu}_{14}\text{Ni}_{12}\text{Sn}_4\text{Nb}_8$ composite.

Phases	Ti (at.%)	Ni (at.%)	Cu (at.%)	Sn (at.%)	Nb (at.%)
Gray dendrite	62.1	2.6	4.8	8.2	22.3
White dendrite	56.3	0.8	0.9	19.4	22.6
Gray matrix	54.3	19.8	19.2	1.6	5.1
Black matrix	61.0	12.9	22.7	0.6	2.8
Average	61.4	12.3	13.8	4.2	8.3

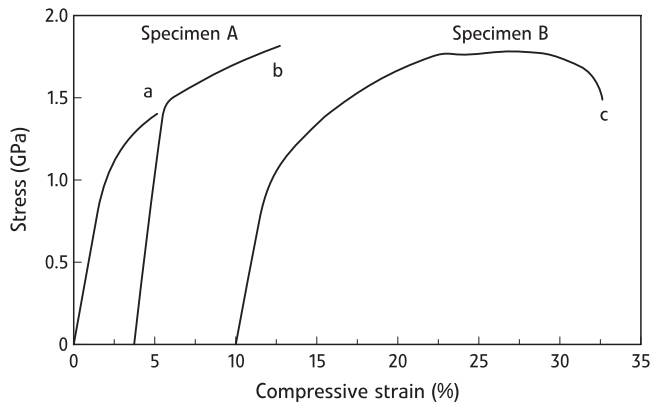


Fig. 3. Compression stress–strain curves for $\text{Ti}_{62}\text{Cu}_{14}\text{Ni}_{12}\text{Sn}_4\text{Nb}_8$ composite. The test was stopped at different strains for SEM observation for specimen A. Specimen B was loaded until fracture. Points **a**, **b** and **c** correspond to total strains of 5 %, 13.5 % and 22.5 %. Note that the data for specimen B are shown at a strain offset of 10 %.

vealed that the white dendrites are a Sn-rich phase while the concentration of the Ti, Cu and Ni elements is lower compared with that of the gray dendritic phase, as shown in Table 1. The SEM images confirm that the volume fraction of the white phase is less than 1 %.

3.2. Mechanical properties

A typical engineering compressive stress–strain curve of the $\text{Ti}_{62}\text{Cu}_{14}\text{Ni}_{12}\text{Sn}_4\text{Nb}_8$ composite is shown in Fig. 3. Unlike monolithic bulk metallic glasses, which exhibit little macroscopic plasticity under compression, the $\text{Ti}_{62}\text{Cu}_{14}\text{Ni}_{12}\text{Sn}_4\text{Nb}_8$ composite exhibits a much higher total strain of ≈ 22 %. During compression, the specimen first becomes buckled followed by fracture. The specimen yields at 1030 MPa, then an obvious work hardening behavior is observed. Young's modulus, as determined from the elastic loading curve, and the compressive plasticity are 56 GPa and 20.7 %, respectively. At a certain strain level after yielding, e. g., point **a** in Fig. 3, the specimen was completely unloaded, and subsequently the deformation features on the specimen surface were observed by SEM. After the SEM observation, the specimen was compressed again. Apparently, the specimen continues to deform along its original stress–strain curve. Another specimen was compressed until fracture without unloading, and the maximum compressive stress is more than 1.8 GPa.

3.3. Surface deformation morphology

Figure 4a shows SEM images (secondary electron (SE) contrast) revealing the deformation features on the specimen surface of the $\text{Ti}_{62}\text{Cu}_{14}\text{Ni}_{12}\text{Sn}_4\text{Nb}_8$ composite deformed up to a total strain of 5 % (point **a** in Fig. 3). Weak (or fine) slip bands can be seen in the dendrites at some local area of the specimen surface, as shown in Fig. 4b. This is a typical deformation feature in the early stage of work hardening for the composite with dendrites, which were never observed previously [18, 21]. However, no deformation can be observed in the matrix at this strain level. These observations validate that the initial deformation originates from dislocation movement and formation of slip bands inside the dendrites. When the specimen is compressed

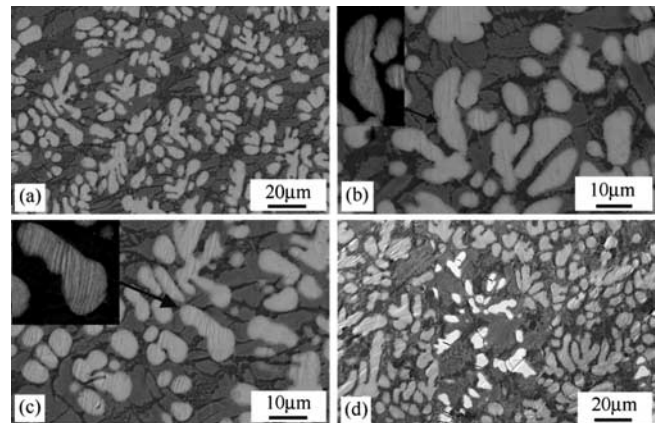


Fig. 4. Scanning electron micrographs (SE contrast) of the specimen surface of the $\text{Ti}_{62}\text{Cu}_{14}\text{Ni}_{12}\text{Sn}_4\text{Nb}_8$ composite at different total strains: (a) low magnification at a total strain of 5 %; (b) slip bands initiate inside the dendrites at 5 % strain with the enlarged inset micrograph of the dendrite indicated by an arrow; (c) more slip bands were formed in the dendrites at 13.5 % strain with the enlarged inset micrograph of the dendrite indicated by an arrow; (d) micro-cracking of the white brittle dendritic phase. The loading axis is horizontal.

further to a strain level of 13.5 % (point **b** in Fig. 3), more slip bands in the dendrites can be found on the specimen surface, as shown in Fig. 4c. These profuse slip bands have rarely been observed in other Ti-based dendrite composites [16, 22]. Besides, the slip bands in these white dendrites are oriented in nearly the same direction (see Fig. 4c). The matrix phase around the dendrites may have a high strength because no shear band or other deformation features were observed at this strain level. Therefore, it is suggested that the work hardening in the stress–strain curve should be mainly attributed to the formation of slip bands inside the dendrites.

At some region on the specimen surface, there are white Sn-rich dendritic particles. It is found that cracking is often nucleated preferentially in these dendrites at the applied total strain of 13.5 %, as shown in Fig. 4d. This indicates that the higher amount of Sn in this phase may cause their embrittlement. This is consistent with the result for other similar Ti-based dendrite-containing nanostructured composites [21, 23].

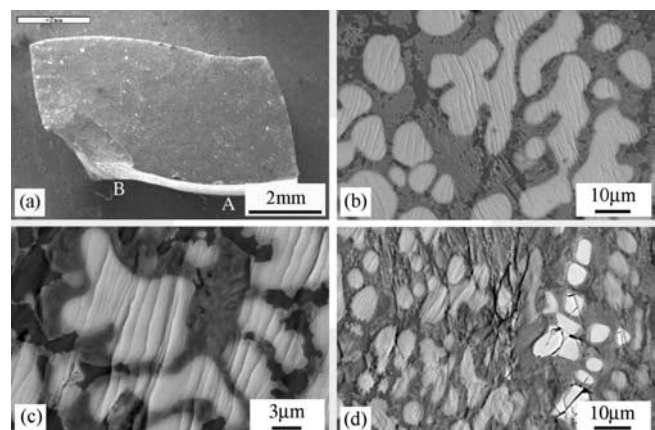


Fig. 5. SEM micrographs (SE contrast) showing: (a) buckling and fracture of the specimen at a total strain of 22.5 %; (b) and (c) dense slip bands formed in the dendrites; (d) further cracking of the white dendritic phase with more Sn. The loading axis is horizontal.

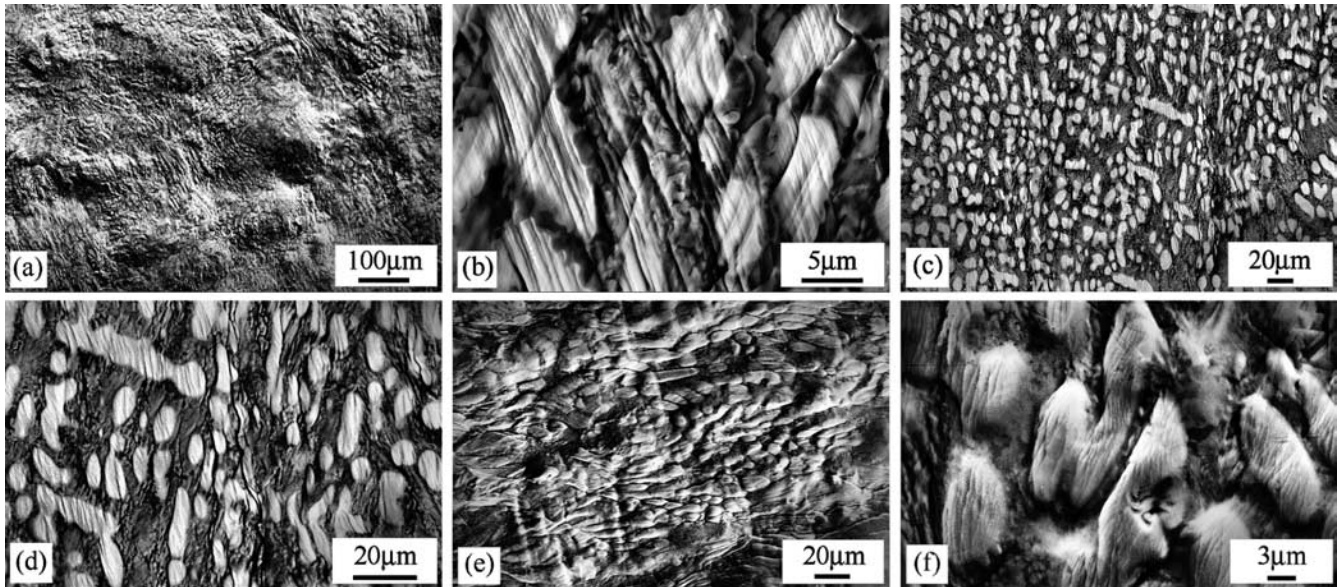


Fig. 6. SEM micrographs (SE contrast) showing severe plastic deformation in a local area near the fracture surface: (a) rough surface morphology corresponding to deformation of the dendrites and the matrix; (b) multiple slip bands inside the dendrites; (c) localized shear band spanning over several dendrites; (d) higher magnification of the shear bands. Note that the shear bands run predominantly through the matrix and at the matrix/dendrite interface. (e) and (f) Deformation of the ductile dendrites. Note that the dendrites are squeezed under compression and protrude from the specimen surface. The loading axis is horizontal except for (e) where it is vertical.

Another specimen was compressed until fracture without unloading. As the load was increased, the specimen becomes buckled and failed at one of the corners, as shown in Fig. 5a. A total strain of 22.5% was obtained when the specimen fractured (point c in Fig. 3). The degree of deformation and the fracture features on the specimen surface are inhomogeneous. Figures 5b and c show the specimen surface with less deformation located far away from the fracture surface, as marked by **A** in Fig. 5a. It seems that the dendrites underwent further work hardening because the slip bands in the dendrites became wider and denser. A small amount of short shear bands can be observed in the matrix between two dendritic arms (Fig. 5c). The shear bands in the matrix are parallel to the slip bands in the dendrites, indicating that the activity of the shear bands in the matrix might be associated with the formation of the slip bands in the dendrites. As shown above, the slip bands inside the dendrites are generated in the early stage of plastic deformation. However, the formation of shear bands in the matrix can be attributed to the impingement of the neighboring slip bands with further work hardening. Besides, the brittle Sn-rich dendrites also undergo further deformation as more cracks were created inside this phase at the final fracture of the specimen (Fig. 5d). However, because the volume fraction of the Sn-rich phase is very low, its contribution to the strength and the plasticity can be neglected.

Severe deformation was observed in an area on the specimen surface near the fracture surface, as marked by **B** in Fig. 5a. This area is characterized by obvious surface relief and wrinkles, which were caused by the severe plastic deformation in both the dendrites and the nanostructured matrix, as shown in Fig. 6a. The compression of the composite at higher strain level may lead to further deformation of the dendrites. Secondary slip bands, oriented along another direction, were formed in addition to the primary slip bands in order to coordinate the plastic deformation as the speci-

men becomes buckled, leading to the formation of multiple slip bands (Fig. 6b).

In addition to the formation of secondary slip bands in the dendrites, a number of localized shear bands were observed in the matrix in this severely deformed area, as shown in Fig. 6c. These shear bands are almost perpendicular to the loading axis and can extend through several dendrites. From an enlarged view of Fig. 6c it can be deduced that these localized shear bands propagate predominantly in the matrix or at dendrite/matrix interfaces, as shown in Fig. 6d. This implies that the shear bands are difficult to pass through the ductile dendrites. We may presume that the strength of the dendrites increases with increasing work hardening, which would normally resist the propagation of the shear bands in the matrix. As the shear bands in the matrix propagate, a stress concentration will build up at the site where the shear bands meet the hardened dendrites, which will trigger the formation of new shear bands in the matrix. Note that the orientation of the shear bands inside the matrix for the Ti-based composite studied here is different from that in some other Zr- or Ti-based dendrite-reinforced composites, in which the shear bands make an angle of about 45° to the compression direction. A rotation mechanism of the shear plane, induced by the very high compressive plasticity, has been suggested and may presumably explain this difference [24].

In the severely deformed area mentioned above, the shape of some dendrite arms changes from an elliptical shape to a flat shape at a direction normal to the load axis, as shown in Fig. 6e. At higher magnification, these dendrites are seen to be squeezed by the compression load and protrude from the specimen surface (see Fig. 6f), reflecting the very high plastic deformability of these dendritic phases. Therefore, the combination of high plasticity and strength of the Ti-based composite may originate from a high degree of deformation in the dendrites and matrix as well as the interactions of the dendrites with the matrix.

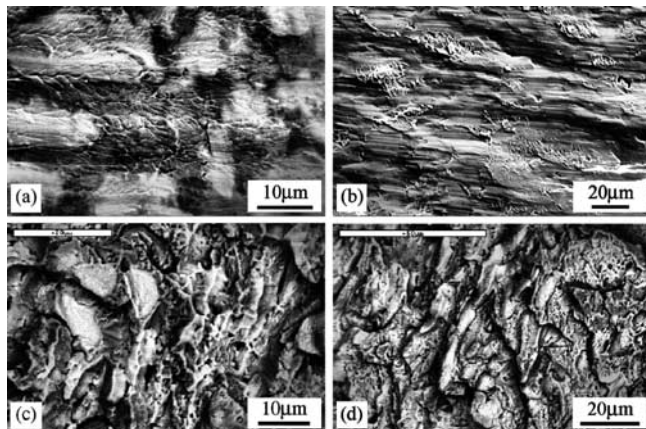


Fig. 7. SEM micrographs (SE contrast) of the fracture surface of the $\text{Ti}_{62}\text{Cu}_{14}\text{Ni}_{12}\text{Sn}_4\text{Nb}_8$ composite: (a) and (b) vein pattern in both dendrites and matrix in a smooth area showing a fast shear fracture, (c) and (d) vein pattern observed in the matrix at another area of the fracture surface.

3.4. Fractographic observations

Figures 7a, b show an area of the fracture surface of the $\text{Ti}_{62}\text{Cu}_{14}\text{Ni}_{12}\text{Sn}_4\text{Nb}_8$ composite after compression to failure. A vein pattern, typical for the viscous flow of metallic glasses [3, 7, 8], can be observed in the smooth region of the fracture surface. Similar smooth fracture surfaces have been observed for the shear fracture of monolithic bulk metallic glasses [12]. Both the dendrites and the matrix are supposed to have undergone a fast fracture as well as local softening or even melting near the fracture surface. In another area of the fracture surface, a rougher surface morphology can be observed, indicating a ductile fracture of the composite. Softening of the composite was not so severe that viscous flow could only be observed in the matrix, as shown in Figs. 7c, d. In this area with rougher surface morphology, no predominant shearing occurs and it is supposed that the ductile fracture proceeds slower than the fast fracture under shear conditions.

The softening or melting phenomenon observed on the fracture surface of a metallic glass may be supposed to originate from the instantaneous release of the stored energy in a highly localized fracture region [25]. The elastic strain energy J stored in a material under compression can be expressed by

$$\frac{J}{\text{m}^3} = \frac{\sigma_F^2}{2E}$$

where σ_F and E are the fracture strength and Young's modulus of the specimen respectively.

The fracture strength of the $\text{Ti}_{62}\text{Cu}_{14}\text{Ni}_{12}\text{Sn}_4\text{Nb}_8$ composite is comparable to that of monolithic metallic glasses, but Young's modulus is smaller than that of metallic glasses [3]. Therefore, the elastic strain energy stored in the composite at fracture is much higher than that of monolithic metallic glasses. Moreover, the low thermal conductivity characteristic for Ti-based alloys [26] also has to be considered. Due to this feature the heat converted from the elastic strain energy stored in the specimen cannot be easily dissipated but renders high enough to induce local melting at the moment of fracture. In this test, two different fracture surface morphologies have been observed in the

$\text{Ti}_{62}\text{Cu}_{14}\text{Ni}_{12}\text{Sn}_4\text{Nb}_8$ composite. The profuse melting trace in the smooth area indicates a fast shear failure, whereas the rougher area with less melting exhibits a slower and ductile fracture with no melting on the dendrites. Therefore, the fast shear fracture combined with the low thermal conductivity of the alloy indicates a concentrated release of the stored elastic strain energy, producing a large amount of adiabatic heating at the moment of fracture. Therefore, the degree of heat conversion from the stored elastic strain energy depends on the fracture mode of the composite. The different areas on the fracture surfaces of the $\text{Ti}_{62}\text{Cu}_{14}\text{Ni}_{12}\text{Sn}_4\text{Nb}_8$ composite (i. e., the smooth and the rougher region) may originate from the complicated stress state in different regions due to the buckling of the specimen during compression.

4. Summary and conclusions

1. A $\text{Ti}_{62}\text{Cu}_{14}\text{Ni}_{12}\text{Sn}_4\text{Nb}_8$ multi-component alloy reinforced with dispersed dendritic phases can be *in-situ* formed by arc-melting. This composite consists of a nanostructured matrix and micrometer-sized dendritic $\beta\text{-Ti(M)}$ ($M = \text{Nb, Sn, Cu and Ni}$) solid solution. During compression, the composite exhibits work hardening after yielding. The maximum strength and plastic strain can be improved to ~ 1.8 GPa and $\sim 21\%$, respectively.
2. In the initial stage of work hardening, the plastic deformation of the Ti-based composite mainly corresponds to the formation of primary slip bands in the dendrites. However, no deformation can be observed in the nanostructured matrix. With further compression, strong work hardening of the composite results in the formation of secondary slip bands in the dendrites, and the activation of shear bands in the matrix. Localized shear bands form and mainly propagate in the matrix or at the matrix/dendrite interface at higher strain level, which might result from the strengthening effect of the dendritic phase. The propagation of the shear bands is resisted by the hardened dendrites.
3. The heat converted from the high elastic strain energy stored in the $\text{Ti}_{62}\text{Cu}_{14}\text{Ni}_{12}\text{Sn}_4\text{Nb}_8$ composite under compression may cause viscous flow during fracture. The fracture surface morphology is multifarious as a result of the complicated stress state of the composite after buckling. A lot of viscous flow traces can be seen in a shear fracture region with smooth morphology, meaning that a large amount of adiabatic heat is produced when the fracture happens in a fast shear mode.

The authors thank M. Adam, F. Baier, M. Branzei, M. Calin, M. Frey, W. Gao, A. L. Greer, M. Heilmaier, U. Kühn, U. Kunz, S. Kuszniski, H. Lehmann, J. J. Lewandowski, W. Löser, N. Radtke, H. Schulze, H. H. Su, J. L. Wen, and G. Yao for technical assistance and a lot of stimulating discussions. This work was supported by the National Natural Science Funds of China (NSFC) under grants Nos. 50401019 and 50323009, and the "Hundred of Talents Project" by the Chinese Academy of Sciences, as well as by the EU within the framework of the RTN Network on Ductile BMG Composites (MRTN-CT-2003-504692).

References

- [1] A. Inoue, T. Zhang, T. Masumoto: Mater. Trans. JIM 30 (1989) 965.
- [2] A. Peker, W.L. Johnson: Appl. Phys. Lett. 63 (1993) 2342.
- [3] W.L. Johnson, A. Inoue, C.T. Liu (Eds.): Bulk Metallic Glasses, Mater. Res. Soc., Warrendale, PA, USA (1999).

- [4] A. Inoue: *Acta Mater.* 48 (2000) 279.
 [5] H.A. Bruck, T. Christman, A.J. Rosakis, W.L. Johnson: *Scripta Mater.* 30 (1994) 429.
 [6] J.H. Schneibel, J.A. Horton, P.R. Munroe: *Metall. Mater. Trans. A* 32 (2001) 2819.
 [7] C.J. Gilbert, V. Schroeder, R.O. Ritchie: *Metall. Mater. Trans. A* 30 (1999) 1739.
 [8] P. Lowhaphandu, J.J. Lewandowski: *Scripta Mater.* 38 (1998) 1811.
 [9] H. Zhang, Z.G. Wang, K.Q. Qiu, Q.S. Zang, H.F. Zhang: *Mater. Sci. Eng. A* 356 (2003) 173.
 [10] C.J. Gilbert, J.M. Lippmann, R.O. Ritchie: *Scripta Mater.* 38 (1998) 537.
 [11] C.J. Gilbert, R.O. Ritchie, W.L. Johnson: *Appl. Phys. Lett.* 71 (1997) 476.
 [12] Z.F. Zhang, J. Eckert, L. Schultz: *Acta Mater.* 51 (2003) 1167.
 [13] Z.F. Zhang, G. He, J. Eckert, L. Schultz: *Phys. Rev. Lett.* 91 (2003) 045505.
 [14] R.D. Conner, R.B. Dandliker, W.L. Johnson: *Acta Mater.* 46 (1998) 6089.
 [15] H. Zhang, Z.F. Zhang, Z.G. Wang, K.Q. Qiu, H.F. Zhang, Q.S. Zang, Z.Q. Hu: *Mater. Sci. Eng.*, 2004, Submitted.
 [16] C.C. Hays, C.P. Kim, W.L. Johnson: *Phys. Rev. Lett.* 84 (2000) 2901.
 [17] F. Szuëcs, C.P. Kim, W.L. Johnson: *Acta Mater.* 49 (2001) 1507.
 [18] G. He, W. Löser, J. Eckert: *Acta Mater.* 51 (2003) 5223.
 [19] Z.F. Zhang, G. He, J. Eckert: *Phil. Mag.* 85 (2005) 897.
 [20] G. He, J. Eckert, W. Löser, L. Schultz: *Nature Mater.* 2 (2003) 33.
 [21] G. He, J. Eckert, W. Löser, M. Hagiwara: *Acta Mater.* 52 (2004) 3035.
 [22] G. He, M. Hagiwara, J. Eckert, W. Löser: *Phil. Mag. Lett.* 84 (2004) 365.
 [23] G. He, J. Eckert, M. Hagiwara: *Metall. Mater. Trans. A* 35 (2004) 3605.
 [24] Z.F. Zhang, G. He, H. Zhang, J. Eckert: *Scripta Mater.* 52 (2005) 945.
 [25] C.T. Liu, L. Heatherly, D.S. Easton, C.A. Carmichael, J.H. Schneibel, C.H. Chen, J.L. Wright, M.H. Yoo, J.A. Horton, A. Inoue: *Metall. Mater. Trans.* 29A (1998) 1811.
 [26] C. Leyens, M. Peters (Eds.): *Titanium and Titanium Alloys*, Wiley-VCH, Weinheim (2003).

(Received December 14, 2004; accepted March 17, 2005)

Correspondence address

Prof. Dr. Zhe-Feng Zhang
 Shenyang National Laboratory for Materials Science
 Institute of Metal Research, Chinese Academy of Sciences
 72 Wenhua Road, Shenyang, 110016, P. R. China
 Tel.: +86 24 2397 1043
 Fax: +86 24 2389 1320
 E-mail: zhfzhang@imr.ac.cn